doi: 10.1038/nature06224

SUPPLEMENTARY INFORMATION

A moonlet belt in Saturn's A ring

Miodrag Sremčević[1]*, Jürgen Schmidt[2], Heikki Salo[3], Martin Seiß[2], Frank Spahn[2], Nicole Albers[1]

[1]Laboratory for Atmospheric and Space Physics, University of Colorado at Boulder, 392 UCB, Boulder CO 80309-0392, USA.

[2]Department of Physics, Nonlinear Dynamics, University of Potsdam, Am Neuen Palais 10, 14469 Potsdam, Germany.

[3]Department of Physical Sciences, Astronomy Division, University of Oulu, Oulu, Finland.

August 28, 2007

File includes:
Supplementary Methods
Supplementary Notes
Supplementary Tables (S1 to S3)
Supplementary Figures and Legends (S1 to S16)

*Corresponding author: phone: +1–303–492–3395, e-mail: Miodrag.Sremcevic@lasp.colorado.edu.

Cassini images

We calibrate the images using standard methods (the `cisscal` software package provided by the Cassini ISS team (*1*), see also refs (*2–4*)). Additionally, the residual horizontal banding present in the α Sco sequence (26 NAC images: N1503229507 ... N1503231007) is further removed by averaging pixels in horizontal direction, similar to the method used for the SOI images with propellers (*2*). The geometry of images is solved using the NAIF Spice toolkit, a NAC field of view of FOV = 6.134 mrad (*1*), and an additional correction to the camera pointing with the α Sco position in the images. This method yields an excellent overlap of ring edges, gaps, as well as density and bending waves in all images (Fig. S1). The geometry of the "movie" sequence of the Encke division (105 NAC images: N1503241997 ... N1503249652) was corrected using the position of the Encke gap edges (*5*). These images have a much better signal-to-noise ratio compared to SOI and α Sco images, and a removal of the residual horizontal banding was not necessary.

Four images in the α Sco sequence exhibit in total seven propeller features (Figs S2–S5). They are listed in Table S1 (labels A to G) where we denote the particular images and, if applicable, their re-occurrence in subsequent images. The re-occurrence is fully consistent with the orbital motion of the features. Another propeller structure is found in one image of the "movie" sequence of the Encke division (Fig. S6).

Dimensions of the propeller features

The method of obtaining the propeller dimensions used in ref. (*2*) is not applicable in the present case, since newly-found propellers contain less pixels compared to those found in the SOI images. Instead, we fit the brightness I/F of the region around the propeller wings to a double Gaussian function

$$\begin{aligned} f(x,y) \;=\; A_0 \quad &+ \quad A_1 \,\exp\left\{ -\left[\frac{x-(x_0-w)}{a}\right]^2 - \left[\frac{y-(y_0+h)}{b}\right]^2 \right\} \\ &+ \quad A_1 \,\exp\left\{ -\left[\frac{x-(x_0+w)}{a}\right]^2 - \left[\frac{y-(y_0-h)}{b}\right]^2 \right\}, \end{aligned} \tag{S1}$$

where x and y are azimuthal and radial coordinates, respectively. The parameters x_0 and y_0 are mere translations of the whole structure in the ring plane. After the fit we use them to correct the semimajor axis $a_0 = a_0' + y_0$ and longitude $l_0 = l_0' + x_0/a_0$ of the moonlet, while the initial coordinate (a_0', l_0') was roughly estimated from the image. Then, $2h$ can be understood as the radial and $2w$ as the azimuthal separation of the two propeller arms. The parameters (a,b) define an ellipse providing the azimuthal and radial size of the arms, while $W = w + a$ is then the total longitudinal extent of one propeller arm. In case a propeller appears in subsequent images we subtract the orbital motion from its longitude x and in this way obtain a second independent fit. A re-projection of the individual features is shown in Figs S7–S9 where the structural fits are indicated. Equation (S1) assumes that the wings of the propeller are symmetric, which is confirmed by the re-projected images.

The difference in shape of the same propeller in two subsequent images, which is apparent for objects B and G, gives an impression of the noise level present in pixel brightness. In particular, the removal of the horizontal banding (2Hz noise) leaves a relatively strong residual pattern.

The fitted parameters for the α Sco features (A to G) are listed in Table S2. For a consistent comparison we also fit the double Gaussian function to the SOI propellers. The corresponding parameters are listed in Table S3. Values for the radial separation of the propeller streaks obtained with our method differ from those of (*2*) by less than 10% (Table S3) and a similarly good agreement is found for the azimuthal separation.

For the propeller structure in Fig. S6 it was necessary to first subtract the Pan-wakes background. The background radial profile $(I/F)(r)$ was obtained by averaging pixels in the azimuthal direction. The wavelength of the resulting wave pattern is fully consistent with the theoretical prediction for the first order Pan wakes (*6*). After subtracting the radial profile, we obtained the following structural fit: $A_0 = 0.014$, $A_1 = 0.0017$, $w = 10.6$km, $h = 0.48$km, $a = 6.2$km, and $b = 1.5$km. However, due to the poor resolution of the image, very long exposure (2s) and thus possible smear, and a potential residual of the Pan wakes imply at least a 50% error in the determined spatial parameters.

The calibration of Cassini ISS images is subject to ongoing effort (*1–4*) and low I/F levels might not be perfectly calibrated. As a measure of uncertainty we check the subtraction of the dark current. Skipping the dark current subtraction for the α Sco sequence increases I/F levels by about 20%, while in case of SOI images I/F levels are almost doubled. This tentatively indicates that I/F levels (that is A_0 and A_1) of the α Sco images are less uncertain.

Streamline crossing and wake damping

Moonlet-induced wakes are characterized by streamlines in a kinematic model developed in ref. (*6*). Streamlines are mass loaded lines characterizing the mean motion of ring matter downstream of the moonlet. Due to the neglect of all particle interactions in this model (*7*), these streamlines can cross. Although the crossing points are fictitious, they mark a location of strong enhancement of the particle number density and collision frequency. In the rings these collisions tend to destroy the phase coherence of particles on the same streamline and scatter the locked eccentricities – two ingredients vital for the existence of wakes. As a result, streamlines become fuzzy and wakes are damped (*8, 9*) near the point of streamline crossing derived from the kinematic model.

The longitude of streamline crossing $\Delta x_{\rm crit}$ reads in terms of the wake wavelength λ_l (*6*)

$$\frac{\Delta x_{\rm crit}}{\lambda_l} = C \left(\frac{|\Delta y|}{H}\right)^3, \qquad C \approx 0.0237, \tag{S2}$$

where $H = a_0[M/(3M_{\rm Saturn})]^{1/3}$ is the moonlet's Hill scale. For a fixed impact parameter $\tilde{y} = |\Delta y|/H$, the right hand side is independent of the moonlet's mass M. Theoretical models suggest a highest density enhancement due to gravitational scattering of the moonlet at $\tilde{y} \approx 4.5$ (*10–12*), yielding a longitude of streamline crossing of $\Delta x_{\rm crit}/\lambda_l \approx 2.2$. This agrees with simulations, where wakes are found to damp after a few cycles (*13, 14*), and is also consistent with the nearly linear scaling of propeller dimensions inferred from observations in this study.

Local N-body ring simulations

Local N-body box simulations (*15–17*) are performed to investigate the formation of propellers and to check the scaling of propeller dimensions derived in the main paper. The simulation method is that of ref. (*17*) using the force method to calculate inelastic impacts. The coefficient of restitution is either constant or velocity dependent (*18*). The self-gravity of ring particles was calculated using a combination of particle-particle and FFT particle-mesh methods. Alternatively, we performed simulations without true self-gravity while mimicking its effect on collision frequency by an enhanced vertical frequency (factor of 3.6) of the particles (*15*). The moonlet is treated as a gravitating particle fixed at the centre of the box. The standard periodic boundary conditions for the box simulation method (*15*) are replaced by open boundaries in tangential direction, where the loss of particles through the downstream boundaries is compensated by an inflow of unperturbed particles at the upstream boundaries taken from a separate simulation without moonlet. For further details about the simulation method see ref. (*13*).

Figure S10 displays a snapshot of a simulation without self-gravity. These simulations were used to compare the expected spatial scalings of detected propellers. Figure S11 demonstrates the linear dependence between the length of the propeller wings *a* and their azimuthal separation *w* derived by the Gaussian fits and comparison to N-body simulations. In the self-gravitating case wake spacings are somewhat modified due to a reduced radial (epicyclic) frequency. However, this does not significantly alter the linear scaling of Fig. S10.

For the calculations of photometric models (next Section) we will use both simulations with and without self-gravity.

Photometric modelling

We have calculated photometric models for the background I/F in α Sco and SOI observing geometries, using standard assumptions for ring particle scattering properties ($n = 3.09$ power law phase function with Bond albedo $\varpi \approx 0.5$ (*19*)). The calculations are made applying the Monte Carlo method (*20*) including multiple scattering up to 50 orders of scattering. The curves in Fig. S12 illustrate two uniform ring models (a classical multilayer model, and a non-gravitating vertically flattened model). Also indicated in the plot are the typical background and propeller I/F (see Table S2). Altogether, the overall difference in I/F levels between the α Sco and SOI images is consistent with the change of viewing geometry. For both cases a "normal" contrast with $d(I/F)/d\tau > 0$ is indicated, for the mid-A ring optical depth $\tau \sim 0.5$.

Figure S12 also illustrates the expected effect of unresolved self-gravity wakes (*21, 22*), which tend to decrease the ring background brightness. Indeed, the region where propellers are seen in the α Sco and SOI images is also the region where the well-known azimuthal brightness asymmetry (*23*) has its maximum in Voyager (*19, 24*) as well as in Hubble Space Telescope images (*25*). It is further the region where UVIS (*26, 27*) and VIMS (*28*) occultation experiments have indicated a strong longitude dependence of ring opacity, similarly interpreted in terms of gravity wakes. The reduced I/F suggests that a part of the reason why moonlet wakes appear so bright is that in these perturbed regions the self-gravity wakes are easily disrupted. If this is the case, then the brightness of moonlet wakes should rise toward the uniform

ring model curves (see the arrows in Fig. S12). In the same picture, the moonlet gaps would be practically indiscernible, provided that their optical depth would be above 0.2 – 0.3. An extra boost to the brightness of gaps and moonlet wakes could also be provided by the enhanced vertical thickness of the perturbed regions, although this effect is not very pronounced (compare the two model curves in Fig. S12). However, the presence of strong self-gravity wakes is clearly not a necessary requirement for the detection of propellers. Namely, the larger ring background I/F for the Encke 'movie' sequence image N1503243458 (Fig. S6) agrees with that expected for a uniform ring. This is consistent with the observations (*25–28*) which indicate a significantly reduced self-gravity wake structure in the region beyond the Encke gap.

We also have constructed synthetic I/F images from simulations for the exact geometry of observations. In Fig. S13 the uppermost two rows display a snapshot from a self-gravitating simulation with a 20m embedded moonlet and the corresponding rectified I/F image. The propeller feature is clearly visible, although not as prominent as in the non-gravitating simulations (*13*). The gap also stands out in this identical particle simulation; additional numerical experiments with a size distribution (but using a smaller calculation region) lead to less prominent gaps and a wider size distribution also tends to decrease the contrast of the moonlet wakes in agreement with ref. (*14*).

An additional factor potentially contributing to the strong contrast of propellers is the release of small - perhaps cm sized - particles in the vicinity of the moonlet due to enhanced impact velocities. In unperturbed regions, the impacts are likely to be rather gentle (a few millimetres per second) and the regolith is held in place by adhesive forces (*29–31*). However, in the vicinity of the moonlet the impact velocities rise considerably: already a 20 meter moonlet can enhance the impact velocities by a factor of 5, which might be enough to release a substantial amount of regolith. Eventually this debris will be absorbed back to particle surfaces, but near the moonlet it could lead to a substantial increase in the optical depth and brightness.

The lowermost two rows in Fig. S13 explore the potential consequences of the release of such debris. Since the direct inclusion of regolith particles to the dynamical simulation is not possible, a faster indirect method is applied: We tabulate the location of fast impacts ($V_{\rm imp} > V_{\rm lim}$) during the actual simulation (the second last row). We then release regolith particles from these impact sites and integrate the debris particle orbits taking into account moonlet's and planet's gravity. The re-absorption is accounted for by checking for impacts with the stored particle positions (using one frozen snapshot; in the end results are averaged using several particle snapshots in turn). To account for the continuous creation of new debris, a steady-state density field is constructed by time averaging over the debris particle orbits. We then assign a fiducial radius to the debris particles (corresponding to an assumed optical depth of free regolith near the moonlet) and make a combined I/F image of particles and regolith debris (last row in Fig. S13).

As shown by Fig. S13, and more quantitatively by Fig. S14, the enhanced I/F levels of propeller features can be accounted for with a modest optical depth of released free debris (here the mean $\tau_{\rm debris} = 0.0025$ is chosen to match the SOI observations). Simultaneously, the contribution of debris to the background I/F is completely negligible, provided that a sufficiently large limiting impact velocity is assumed (here $V_{\rm lim} = 1{\rm cms}^{-1}$); altogether the model is not sensitive to the exact parameter values chosen. Also note that the brightness contrast enhancement due to debris works equally well in the absence of background self-gravity wakes (lower frame of Fig. S14). In this framework there is thus no reason to believe that the presence/non-presence of gravity wakes would cause significant bias on the detection of propellers.

Break-up hypothesis and belt width

As it has been already suggested in ref. (*2*), the break-up hypothesis seems the most likely explanation of the propellers' origin. While the steepness of the size distribution and the very existence of the belt strongly support the break-up hypothesis, a challenge remains to explain the belt width of about 3000 km, if all propellers are remnants of one single moon.

We performed a simple numerical experiment, assuming that after break-up the fragments are released in random directions with a typical speed $\langle v_{\rm ejecta} \rangle$ from the position of the progenitor moon, and recorded the spread of semi-major axes Δa and the maximal spread of all orbits Δr (i.e. the difference between maximum of all apocentres and minimum of all pericentres). Assuming a target moon on a circular orbit ($e_0 = 0$) at 130,000 km distance from Saturn and typical fragment release speeds of $\langle v_{\rm ejecta} \rangle = 5$, 10, 20, 50 and 100 $\mathrm{m\,s^{-1}}$ we obtain $\Delta r = 300$, 610, 1220, 3050 and 6090 km, respectively, while $\Delta a \approx \Delta r/2$. All of the tested speeds were reported in the literature in various scenarios for catastrophic breakup (*32–34*). Since the impactors are likely to come from outside the Saturnian system, the impact velocities are indeed expected to be large after gravitational focusing, and even larger ejecta speeds appear plausible. If the target moon was initially on an elliptical orbit ($e_0 > 10^{-3}$) the resulting spread of the fragments is even stronger. Collisions of the fragments and grinding by meteoroids could even further spread the shards in the ring plane.

Moreover, if the target moon was of Pan size or larger, it necessarily resided in a wide gap in the rings. After the catastrophe, the gap begins to close by viscous diffusion, the edges slowly approaching each other. This would lead to trapping of the moon fragments at the edges preferentially at their pericentres and apocentres. The enhanced energy input at the edges may increase the rate of gap closure. An interesting possibility is that this scenario introduces propeller sub-belts at places where fragments were trapped by the closing edges. In Figure S15 we show the distribution of radii of capture of the fragments by the closing edges for the example of a mean ejection speed $\langle v_{\rm ejecta} \rangle = 50\,\mathrm{m\,s^{-1}}$ and a target moon on a circular orbit. Here, fragments are assumed to be trapped in the closing ring at their apocentre, if their semi-major axis is larger than the one of the progenitor moon, or at their pericentre, if their semi-major axis is smaller. While the current statistics of detected propellers is not sufficient to be certain, the observed propellers do seem concentrated in at least two sub-regions (Fig. S16).

Moonlet belt lifetimes

In order to estimate the lifetime of a moonlet belt we start with a Smoluchowski type equation

$$\frac{\mathrm{d}n_d(s,t)}{\mathrm{d}t} = +(\mathrm{GAIN}) \; -(\mathrm{LOSS}), \tag{S3}$$

where $n_d(s,t)$ is the differential size distribution of moonlets and ring particles. Note that although Smoluchowski type equations are commonly used for coagulation processes the underlying kinetic concept provides a general tool to explore erosive processes as well (*35*). If we consider impacts by meteoroids only, the loss term can be written as

$$(\mathrm{LOSS}) = n_d(s,t)\; \sigma(s)\; J(s), \tag{S4}$$

where $\sigma(s) = \pi s^2$ is the cross section, and $J(s)$ is the flux of all impactors $s_{\rm imp} > s_{\rm crit}(s)$ which are able to destroy the target of the size s. Then, the gain term describes the increase of $n_d(s,t)$ due to the fragments after the impact.

Here we will simplify the integro-differential equation (S3) by assuming $({\rm GAIN}) = 0$. This is strictly valid for moonlets larger than the largest fragment created in all impacts. From Fig. 4 we expect that there are no moonlets larger than 150 m, and since typically the largest fragments are a few times smaller than the target, we conclude that the assumption $({\rm GAIN}) = 0$ is still valid for moonlets $s > 50$ m. Then, Eq. (S3) admits a simple solution $n_d(s,t) = n_d(s,0)\exp[-\sigma(s)\,J(s)\,t]$. Furthermore we can calculate the needed time T to completely destroy all moonlets larger than s_m from the total number of all particles being less than one

$$1 \geq \int_{s_m}^{\infty} n_d(s,T)\,\Sigma\,ds, \tag{S5}$$

where $\Sigma \approx 3.3 \times 10^9\,{\rm km}^2$ is the total moonlet belt area. The integral reduces to an algebraic equation, which we solve numerically. We use fluxes as given in ref. (*36*), and strength properties as provided in ref. (*32*) Then, the needed time to destroy all moonlets larger than $s > s_m = 50$ m from the belt shown in Fig. 4 is $T = 3.0 \times 10^8$ years, or for $s > s_m = 90$ m it is $T = 1.1 \times 10^8$ years. The poorly constrained meteoroid fluxes and uncertainties in the fragmentation physics imply at least an order of magnitude uncertainty in these estimates.

References

1. Porco, C. C. *et al.* Cassini imaging science: Instrument characteristics and anticipated scientific investigations at Saturn. *Space Sci. Rev.* **115**, 363–497 (2004).

2. Tiscareno, M. S. *et al.* 100-metre-diameter moonlets in Saturn's A ring from observations of propeller structures. *Nature* **440**, 648–650 (2006).

3. Tiscareno, M. S., Burns, J. A., Nicholson, P. D., Hedman, M. M. & Porco, C. C. Cassini imaging of Saturn's rings. *Icarus* **189**, 14–34 (2007).

4. Hedman, M. M. *et al.* Saturn's dynamic D ring. *Icarus* **188**, 89–107 (2007).

5. French, R. G. *et al.* Geometry of the Saturn system from the 3 July 1989 occultation of 28 Sgr and Voyager observations. *Icarus* **103**, 163–214 (1993).

6. Showalter, M. R., Cuzzi, J. N., Marouf, E. A. & Esposito, L. W. Satellite 'wakes' and the orbit of the Encke Gap moonlet. *Icarus* **66**, 297–323 (1986).

7. Stewart, G. R. Nonlinear satellite wakes in planetary rings. I - Phase-space kinematics. *Icarus* **94**, 436–450 (1991).

8. Borderies, N., Goldreich, P. & Tremaine, S. The formation of sharp edges in planetary rings by nearby satellites. *Icarus* **80**, 344–360 (1989).

9. Lewis, M. C. & Stewart, G. R. Collisional dynamics of perturbed planetary rings. I. *Astron. J.* **120**, 3295–3310 (2000).

10. Spahn, F. & Wiebicke, H. J. Long-term gravitational influence of moonlets in planetary rings. *Icarus* **77**, 124–134 (1989).

11. Spahn, F. & Sremčević, M. Density patterns induced by small moonlets in Saturn's rings? *Astron. Astrophys.* **358**, 368–372 (2000).

12. Sremčević, M., Spahn, F. & Duschl, W. J. Density structures in perturbed thin cold discs. *Mon. Not. R. Astron. Soc.* **337**, 1139–1152 (2002).

13. Seiß, M., Spahn, F., Sremčević, M. & Salo, H. Structures induced by small moonlets in Saturn's rings: Implications for the Cassini Mission. *Geophys. Res. Lett.* **32**, 11205–+ (2005).

14. Lewis, M. C. & Stewart, G. R. Features around embedded moonlets in Saturn's rings: The role of self-gravity and particle size distributions. *submitted to Icarus* (2007).

15. Wisdom, J. & Tremaine, S. Local simulations of planetary rings. *Astron. J.* **95**, 925–940 (1988).

16. Salo, H. Numerical simulations of dense collisional systems. *Icarus* **90**, 254–270 (1991).

17. Salo, H. Simulations of dense planetary rings. III. Self-gravitating identical particles. *Icarus* **117**, 287–312 (1995).

18. Bridges, F., Hatzes, A. & Lin, D. Structure, stability and evolution of Saturn's rings. *Nature* **309**, 333–338 (1984).

19. Dones, L., Cuzzi, J. N. & Showalter, M. R. Voyager photometry of Saturn's A Ring. *Icarus* **105**, 184–215 (1993).

20. Salo, H. & Karjalainen. Photometric modeling of Saturn's rings: I. Monte Carlo method and the effect of nonzero volume filling factor. *Icarus* **164**, 428 (2003).

21. Julian, W. H. & Toomre, A. Non-axisymmetric responses of differentially rotating disks of stars. *Astrophys. J.* **146**, 810–830 (1966).

22. Salo, H. Gravitational wakes in Saturn's rings. *Nature* **359**, 619–621 (1992).

23. Camichel, H. Mesures photométriques de Saturne et de son anneau. *Annales d'Astrophysique* **21**, 231–242 (1958).

24. Franklin, F. A. *et al.* Voyager observations of the azimuthal brightness variations in Saturn's rings. *Icarus* **69**, 280–296 (1987).

25. French, R. G., Salo, H., McGhee, C. A. & Dones, L. HST observations of azimuthal asymmetry in Saturn's rings. *Icarus* **189**, 493–522 (2007).

26. Colwell, J. E., Esposito, L. W. & Sremčević, M. Self-gravity wakes in Saturn's A ring measured by stellar occultations from Cassini. *Geophys. Res. Lett.* **33**, 7201–+ (2006).

27. Colwell, J. E., Esposito, L. W., Sremčević, M., Stewart, G. R. & McClintock, W. E. Self-Gravity wakes and radial structure of Saturn's B ring. *Icarus, doi:10.1016/j.icarus.2007.03.018* (2007).

28. Hedman, M. M. *et al.* Self-Gravity Wake Structures in Saturn's A Ring Revealed by Cassini VIMS. *Astron. J.* **133**, 2624–2629 (2007).

29. Weidenschilling, S. J., Chapman, C. R., Davis, D. R. & Greenberg, R. Ring particles - Collisional interactions and physical nature. In *Planetary Rings*, 367–415 (1984).

30. Albers, N. & Spahn, F. The influence of particle adhesion on the stability of agglomerates in Saturn's rings. *Icarus* **181**, 292–301 (2006).

31. Albers, N. *On the relevance of particle adhesion: Applications to Saturn's rings*. Ph.D. thesis, University of Potsdam, Germany (2006).

32. Benz, W. & Asphaug, E. Catastrophic Disruptions Revisited. *Icarus* **142**, 5–20 (1999).

33. Michel, P., Benz, W., Tanga, P. & Richardson, D. C. Collisions and Gravitational Reaccumulation: Forming Asteroid Families and Satellites. *Science* **294**, 1696–1700 (2001).

34. Michel, P., Tanga, P., Benz, W. & Richardson, D. C. Formation of Asteroid Families by Catastrophic Disruption: Simulations with Fragmentation and Gravitational Reaccumulation. *Icarus* **160**, 10–23 (2002).

35. Spahn, F., Albers, N., Sremcevic, M. & Thornton, C. Kinetic description of coagulation and fragmentation in dilute granular particle ensembles. *Europhysics Letters* **67**, 545–551 (2004).

36. Cuzzi, J. N. & Estrada, P. R. Compositional Evolution of Saturn's Rings Due to Meteoroid Bombardment. *Icarus* **132**, 1–35 (1998).

37. Salo, H., Karjalainen, R. & French, R. G. Photometric modeling of Saturn's rings. II. Azimuthal asymmetry in reflected and transmitted light. *Icarus* **170**, 70–90 (2004).

ID	First image	Subsequent image	re-projection
A	N1503229987 (Fig S2, red)	N1503230047 (Fig S3, red)	Fig S7 (top)
B	N1503229987 (Fig S2, blue)	N1503230047 (Fig S3, blue)	Fig S7 (bottom)
C	N1503229987 (Fig S2, magenta)	N/A[a]	Fig S8 (top)
D	N1503229987 (Fig S2, yellow)	N/A[a]	Fig S8 (middle)
E	N1503230227 (Fig S4, red)	N1503230287 (Fig S5, red)	Fig S8 (bottom)
F	N1503230227 (Fig S4, blue)	N1503230287 (Fig S5, blue)	Fig S9 (top)
G	N1503230227 (Fig S4, magenta)	N1503230287 (Fig S5, magenta)	Fig S9 (bottom)

(a) The subsequent image does not cover the particular region (Kepler motion subtracted).

Table S1: Propeller features and their references to figures in this supplement. For their distinction they are encircled in given colours.

ID	NAC image	a_0[a] [km]	l_0[b] [deg]	A_0	A_1	w[c] [m]	h [m]	a[c] [m]	b[c] [m]
A	N1503229987	131524.9	280.6339	0.0088	0.0029	4600	341± 38	3620	1260
A	N1503230047	131524.8	280.6339	0.0088	0.0034	4340	445± 36	3130	1300
B	N1503229987	131388.9	280.7723	0.0085	0.0020	2500	281± 66	2320	1060
C	N1503229987	131508.7	280.8432	0.0086	0.0025	2300	312± 64	1490	1100
D	N1503229987	131657.4	280.8156	0.0091	0.0024	3900	350± 52	3000	1340
E	N1503230227	128851.0	282.1649	0.0067	0.0016	2750	102±110	2570	1980
E	N1503230287	128851.2	282.1649	0.0068	0.0020	2970	52± 83	2460	1790
F	N1503230227	128833.1	282.1793	0.0067	0.0018	2720	234± 96	1810	1520
F	N1503230287	128833.1	282.1796	0.0068	0.0021	2740	327± 72	1980	1270
G	N1503230287	128786.8	282.1885	0.0067	0.0020	2350	240± 80	2340	1430

(a) Nominal error of a_0 is half pixel size: ± 0.5 km. (b) Nominal error of l_0 is half pixel size: $\pm 0.0002°$.
(c) Error obtained in the fitting procedure is at maximum 10%.

Table S2: Fitted parameters of the propellers providing their location (a_0, l_0) and extent (w, h). Only successful fits are listed.

ID	NAC image	a_0 [km]	A_0	A_1	w [m]	h [m]	$\Delta r/2$[a] [m]	a [m]	b [m]
SOI1	N1467347210	129499.77	0.0035	0.0051	1590	184±5	173	1110	160
SOI2	N1467347249	130101.25	0.0042	0.0052	1180	147±5	137	800	130
SOI3	N1467347249	130120.77	0.0043	0.0044	930	147±7	139	530	140
SOI4	N1467347249	130128.61	0.0041	0.0047	830	131±6	135	630	130

(a) Radial separation derived in ref. (*2*).

Table S3: Fitted parameters of the SOI propellers.

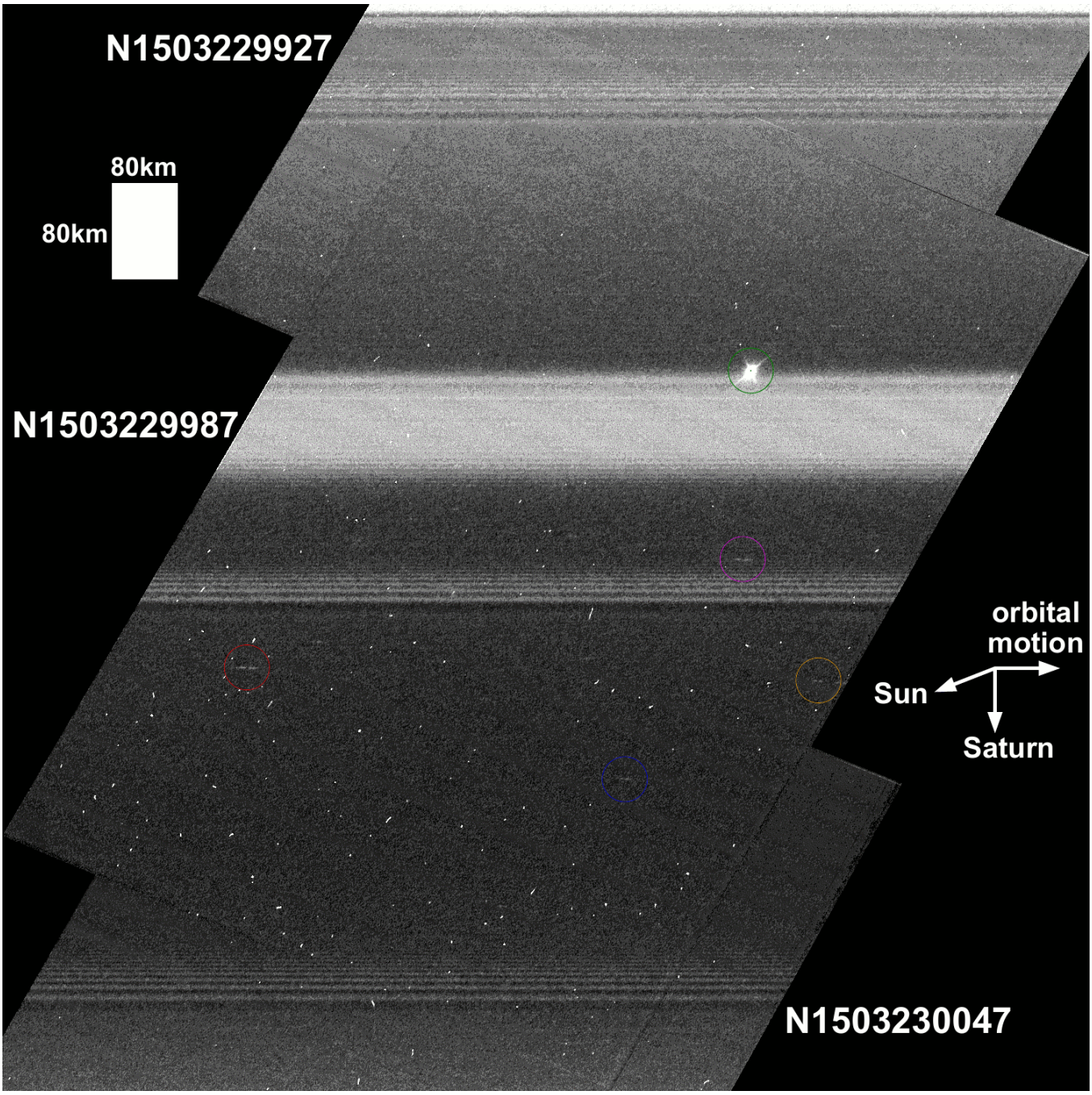

Figure S1: Image N1503229987 (Fig. S2) re-projected and merged with subsequent (N1503230047, Fig. S3) and preceding image (N1503229927). We subtracted the orbital motion for merging the pictures. Horizontal coordinate is azimuth (orbital motion is to the right), and vertical coordinate is distance from Saturn.

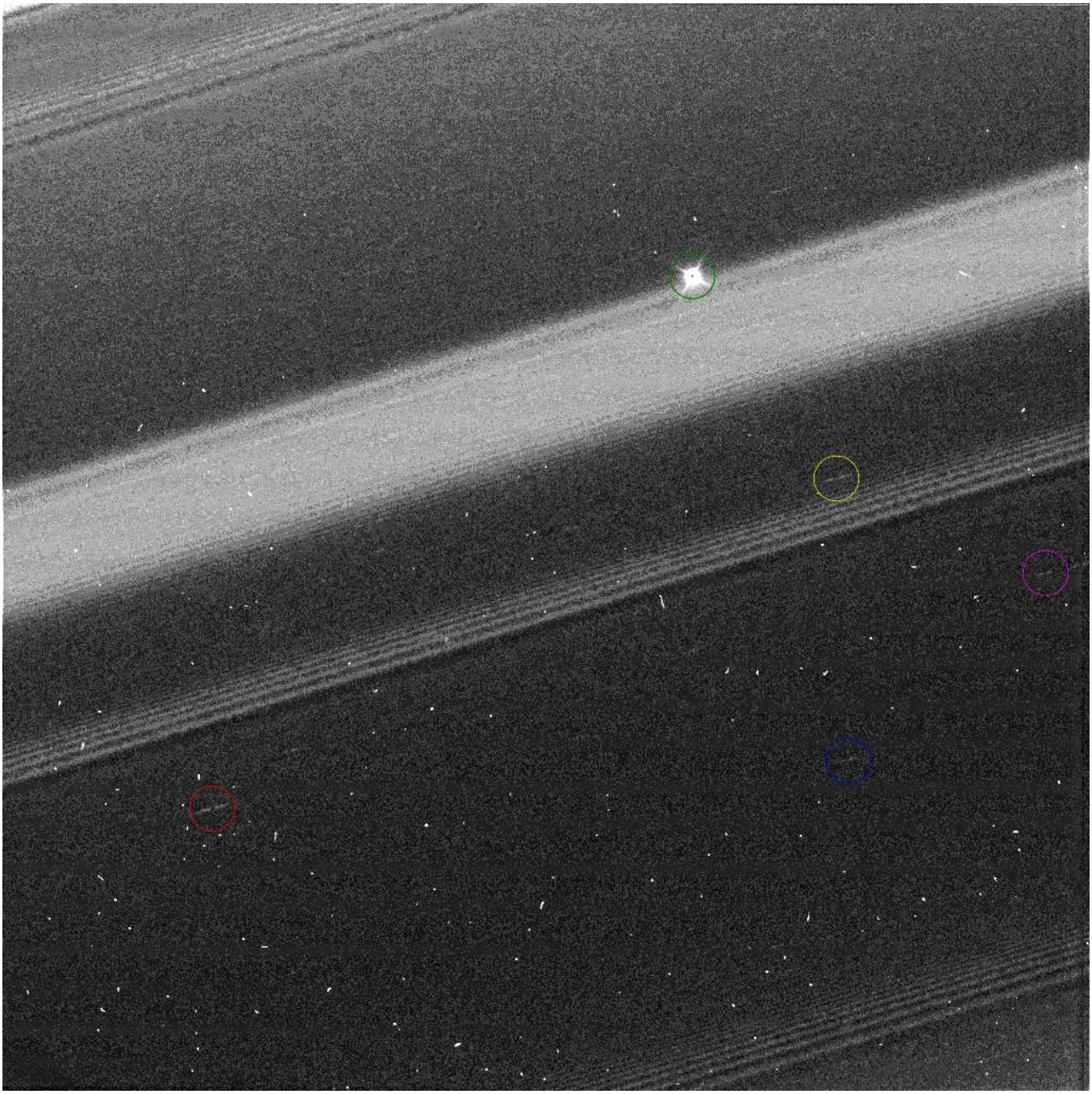

Figure S2: Image N1503229987 taken in clear filter (CL1/CL2) with 50ms exposure on 2005-08-20T11:25:00 UTC (Fig. 1 of the main paper displays the central portion of this image). The grey-scale colour represents I/F in the range of $[0.0071, 0.0167]$. The brightest spot, encircled in green, is the star α Sco occulted by the rings. Four of the new propeller features are clearly visible in this image, encircled in different colours to facilitate comparison. The image was taken from a distance of $216,400$km from Saturn with a phase angle of 127.8°, $B_{\rm Sun} = 20.67^\circ$, $\phi_{\rm Sun} = -104.7^\circ$, $B_{\rm Cassini} = 32.08^\circ$, and $\phi_{\rm Cassini} = 17.8^\circ$, where elevation B is measured from the ring plane and longitude ϕ from the radial direction ($\phi = 90^\circ$ is orbital motion). The picture resolution is 1055×506m per pixel (radial $\times$ azimuthal) covering $131,007$ – $132,338$km from Saturn.

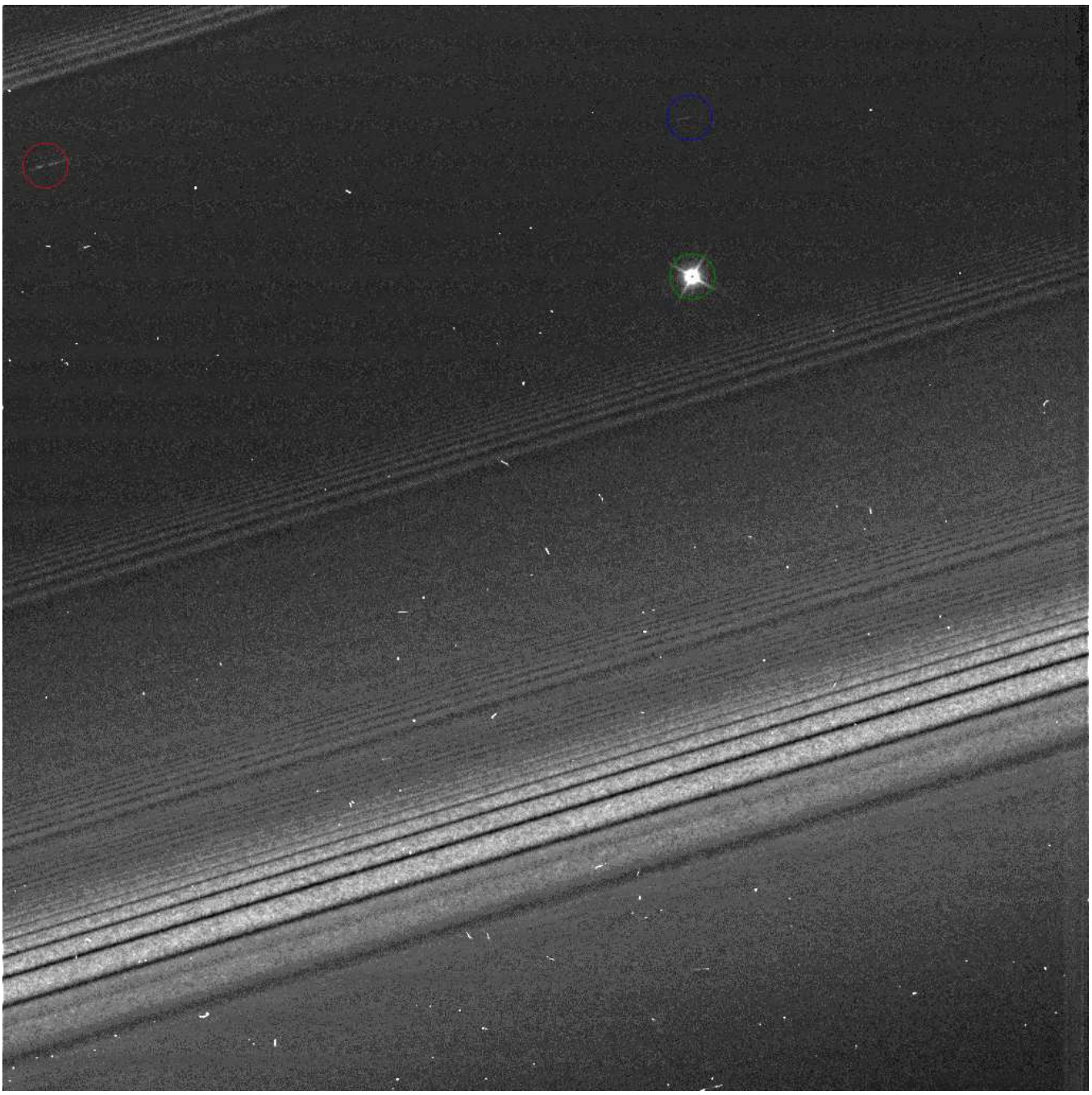

Figure S3: Image N1503230047 subsequent (+60 seconds) to the image in Fig. S2 . The grey-scale colour represents I/F in the range of $[0.0060, 0.0210]$. Two of seven propeller features are visible and encircled in red and blue colour. These can be identified as two of the features in Fig. S2 (where the same colour code was used) as their location is consistent with their orbital motion. The image resolution is 1063×511m per pixel (radial $\times$ azimuthal) covering $130,350$ – $131,688$km from Saturn.

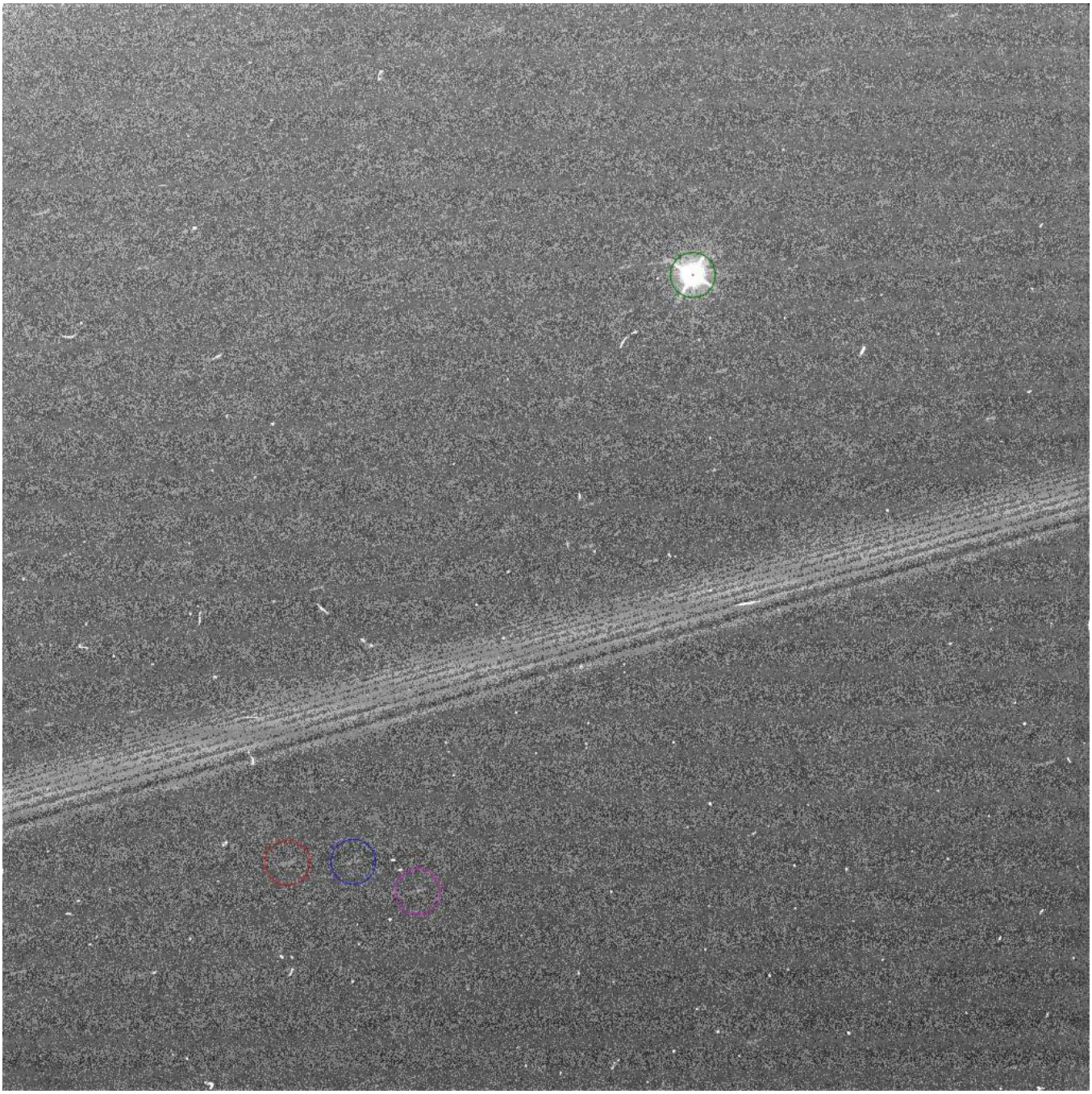

Figure S4: Image N1503230227 taken on 2005-08-20T11:29:00 UTC. The grey-scale colour represents I/F in the range of $[0.0043, 0.0103]$. This image reveals three of the seven propeller features. The image resolution is 1087×527m per pixel (radial $\times$ azimuthal) covering $128,403$ – $129,763$km from Saturn.

Figure S5: Image N1503230287 subsequent (+60 seconds) to the image from Fig. S4. The grey-scale colour represents I/F in the range of $[0.0041, 0.0101]$. It shows three propeller features marked by coloured circles. The same features appear in Fig. S4 marked in identical colour. The image resolution is 1096×532m per pixel (radial $\times$ azimuthal) covering $127,763$ – $129,131$km from Saturn.

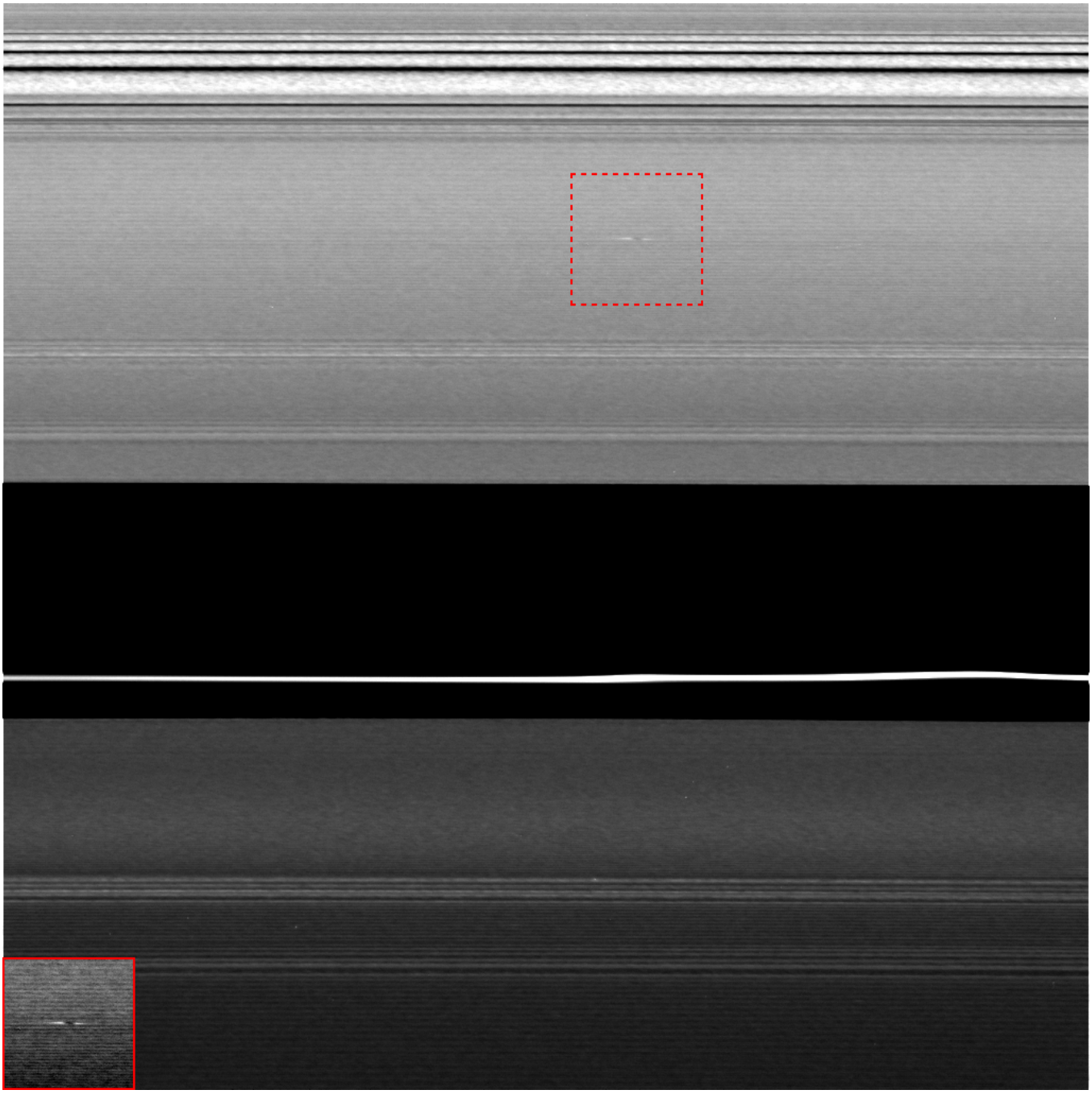

Figure S6: Image N1503243458 taken in clear filter (CL1/CL2) with 2s exposure on 2005-08-20T15:09:30 UTC. The grey-scale colour represents I/F in the range of $[0.008, 0.019]$. Enclosed in red is one of the new propeller features (inset at the bottom shows contrast enhanced area). The overlap between the images in this sequence is not complete and the propeller structure is not repeated in other images. The image was taken from a distance of $272,700$km from Saturn with the phase angle of 162.3°, $B_{\rm Sun} = 20.67^\circ$, $\phi_{\rm Sun} = -151.4^\circ$, $B_{\rm Cassini} = 37.88^\circ$, and $\phi_{\rm Cassini} = 33.3^\circ$. The picture resolution is 1448×1133m per pixel (radial $\times$ azimuthal) covering $132,914$ – $134,400$km from Saturn. In the image Saturn is towards the bottom while the orbital motion is to the right. The moon Pan orbits in the Encke division, the dark stripe in the middle, and is 165° upstream from the centre of the image. Its first order wakes are seen in the image as fine parallel stripes below and above the Encke gap.

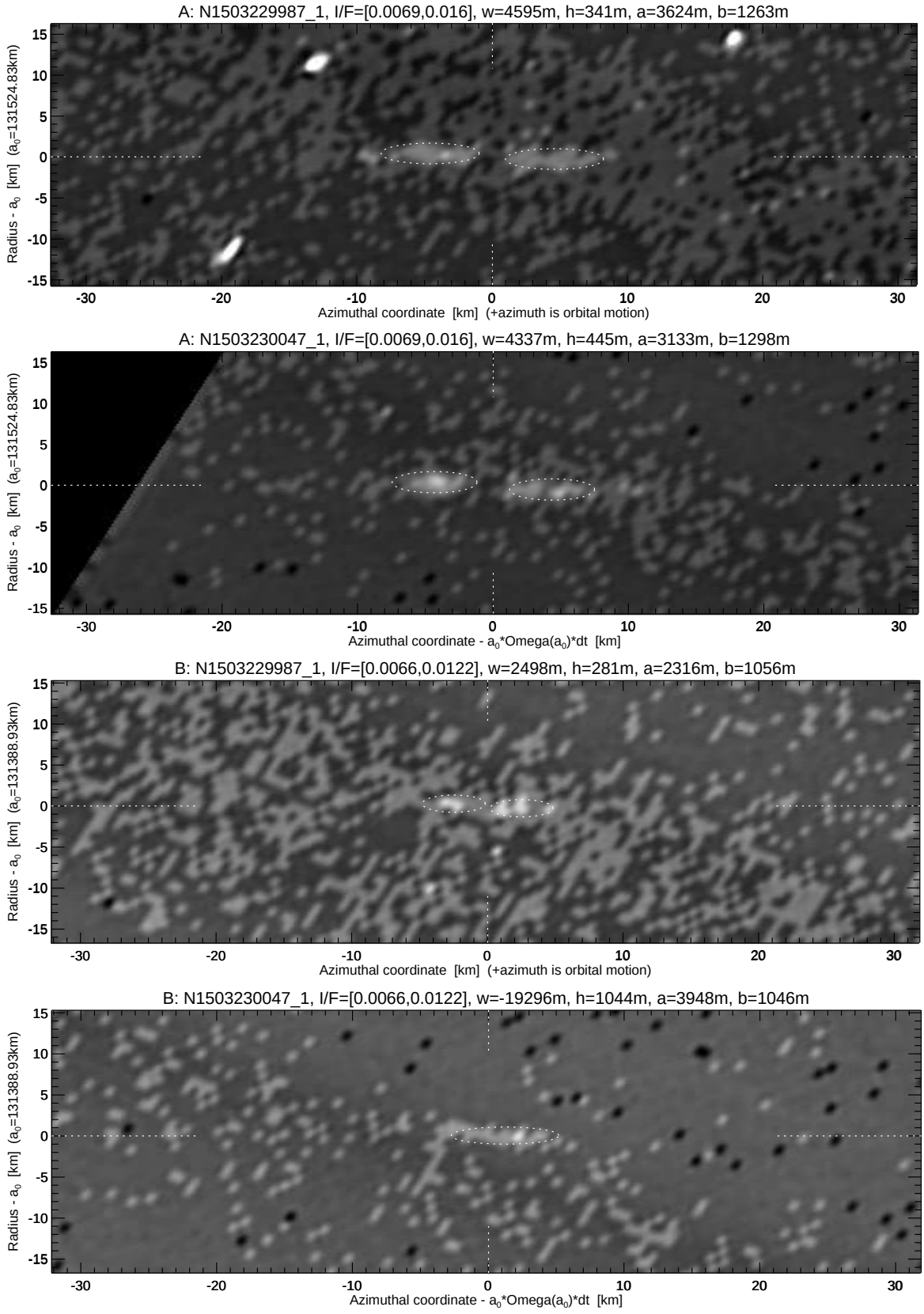

Figure S7: Propellers A (top) and B (bottom) in $(x = a_0\phi, y = r)$ re-projected space. $+x$ coordinate is the direction of orbital motion.

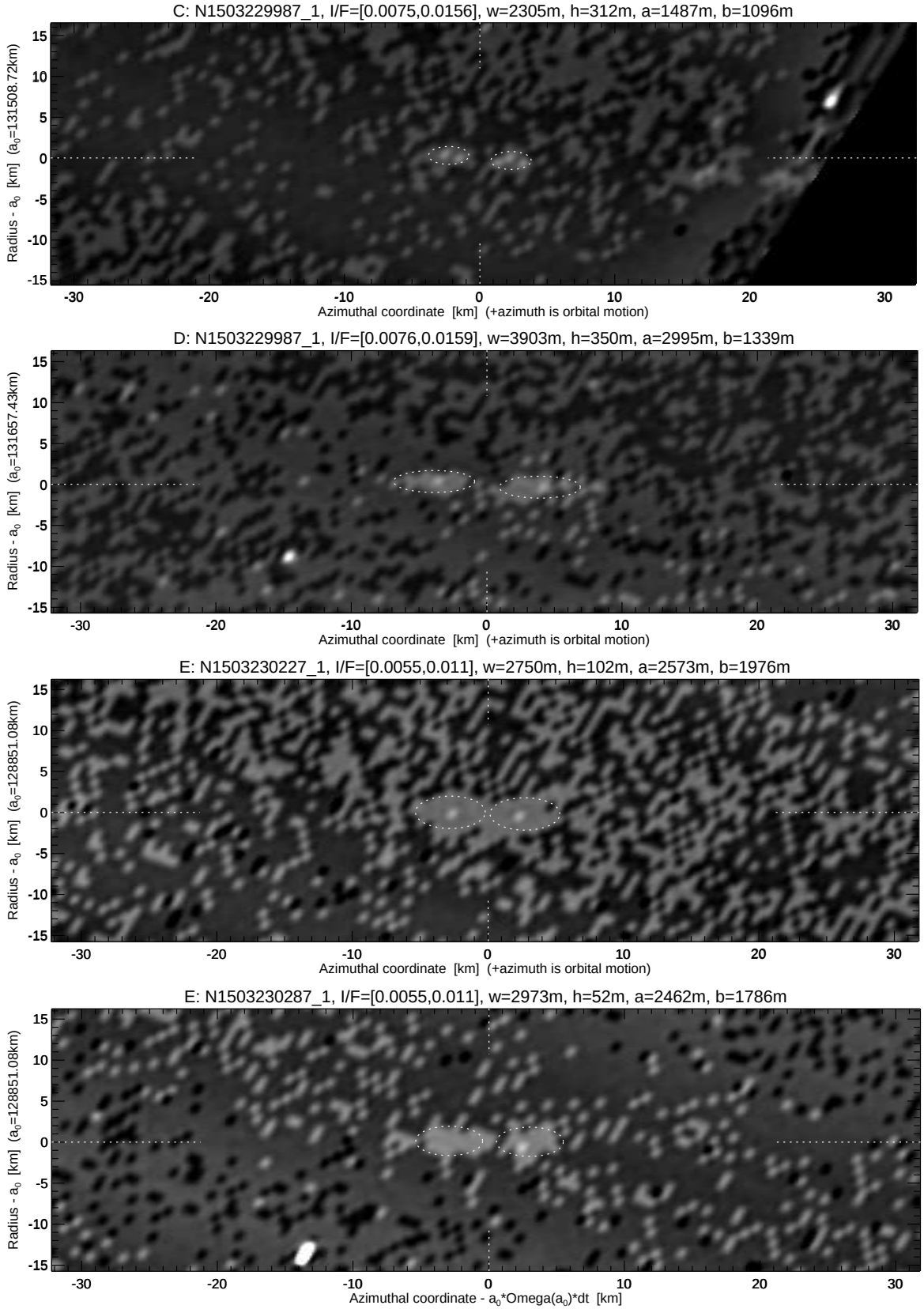

Figure S8: Propellers C (top), D (second from top), E (bottom two figures).

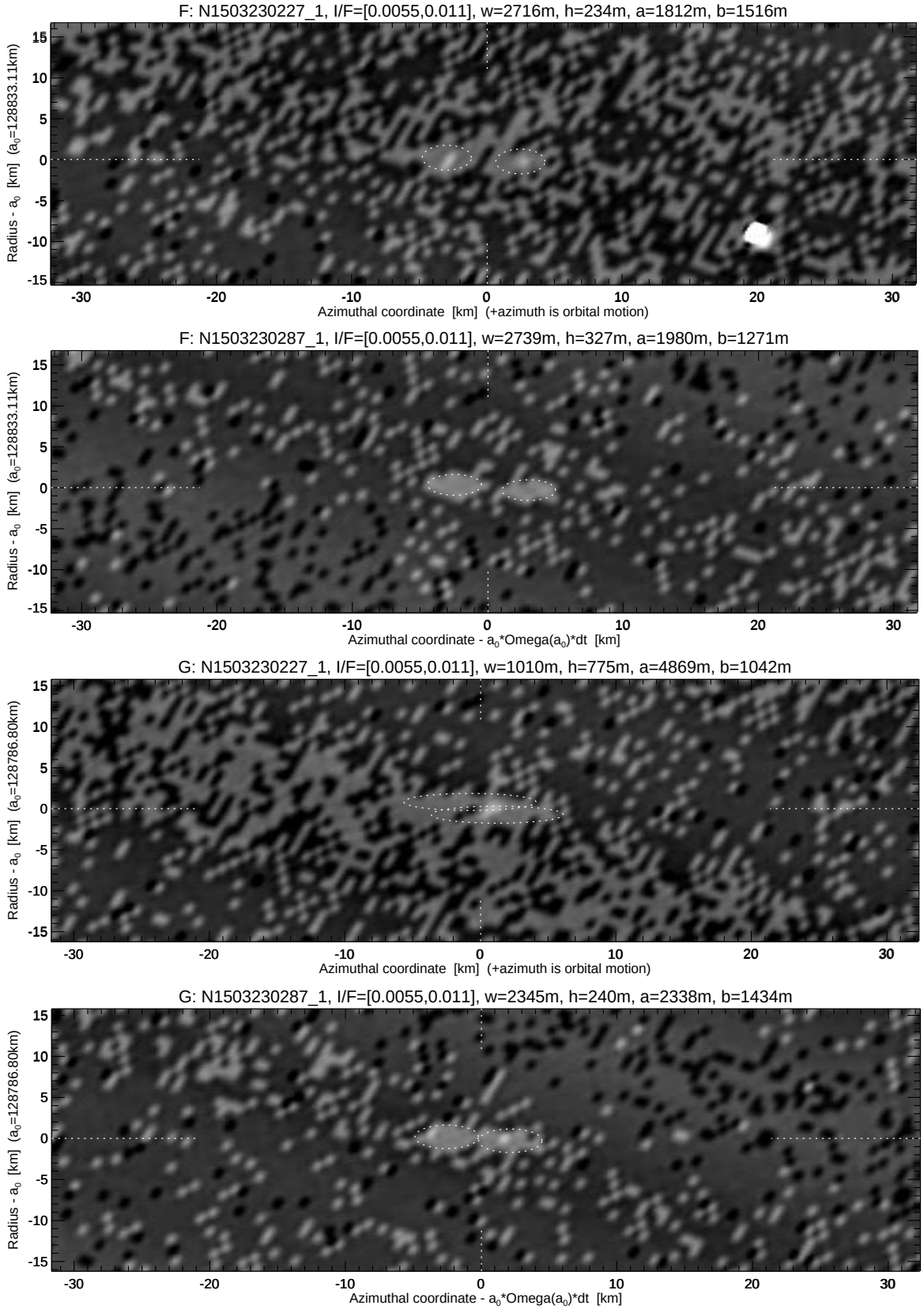

Figure S9: Propellers F (top) and G (bottom).

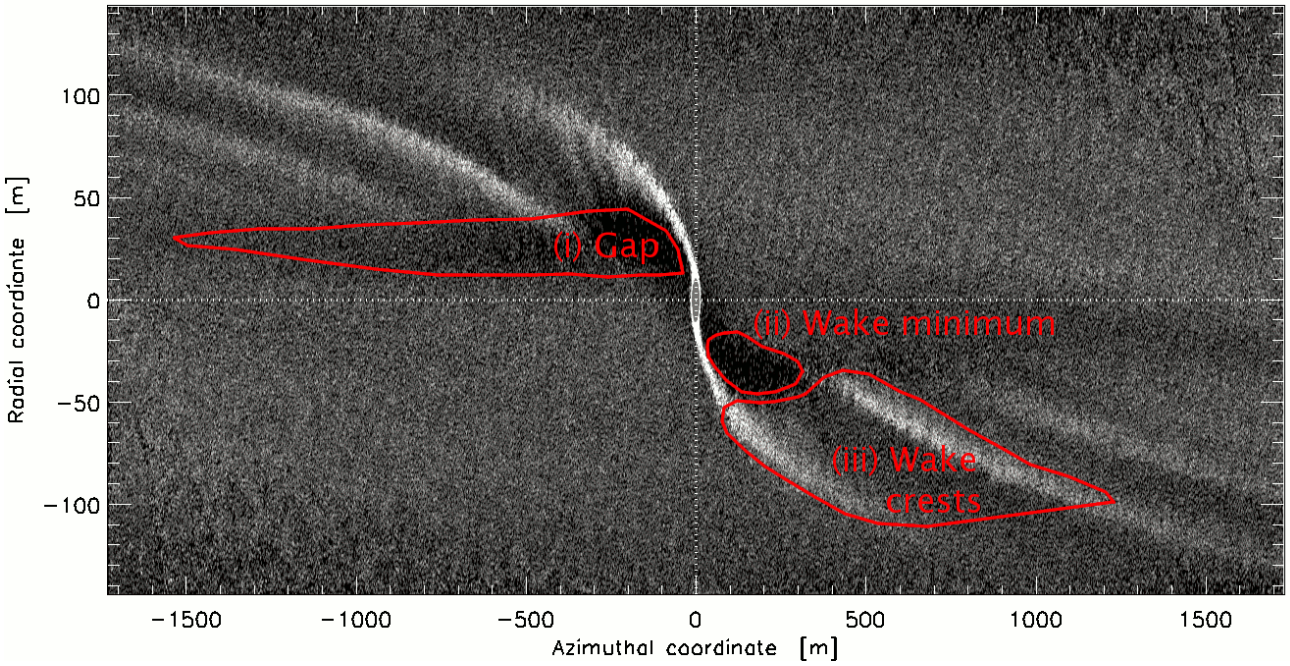

Figure S10: Snapshot of an N-body simulation of a planetary ring with an embedded moonlet of radius $R_{\rm moon} = 12\,{\rm m}$. The grey-scale is proportional to the surface density of the ring. The simulation without self-gravity includes 200,000 particles of one meter radius with a normal geometrical optical depth of $\tau_{\rm dyn} = 0.63$. A constant coefficient of restitution of $\varepsilon = 0.5$ was used. In the foreground we illustrate three possible interpretations of bright propeller wings in images: (i) Incomplete gaps opened by a moonlet (*11, 12*). (ii) Density minima of the moonlet induced wakes. (iii) Density maxima of the moonlet induced wakes. Large moons, like Pan and Daphnis, are able to open a complete gap while small moons leave trailing and leading regions of depleted and enhanced density.

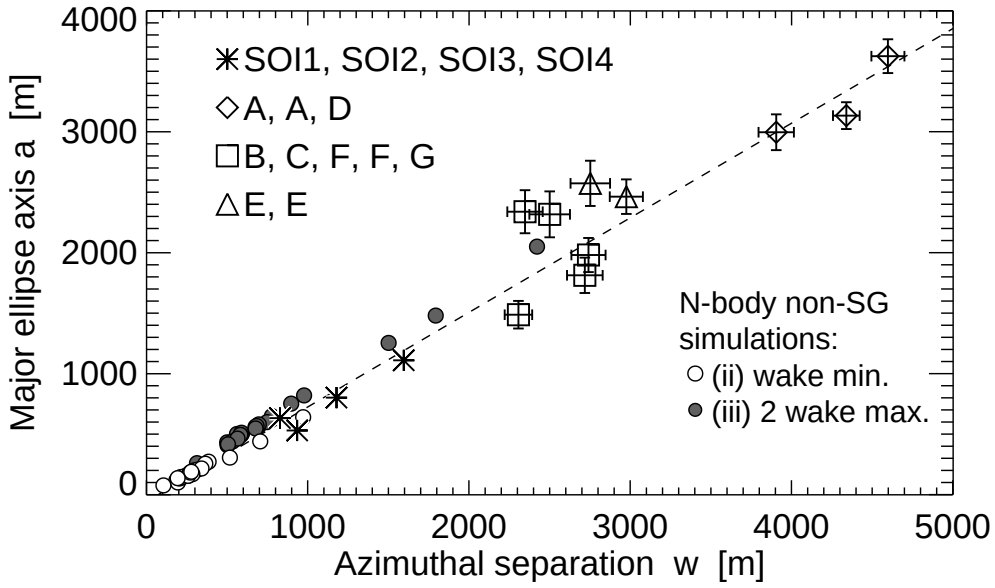

Figure S11: Major axis of the fitted ellipse a as a function of azimuthal separation w.

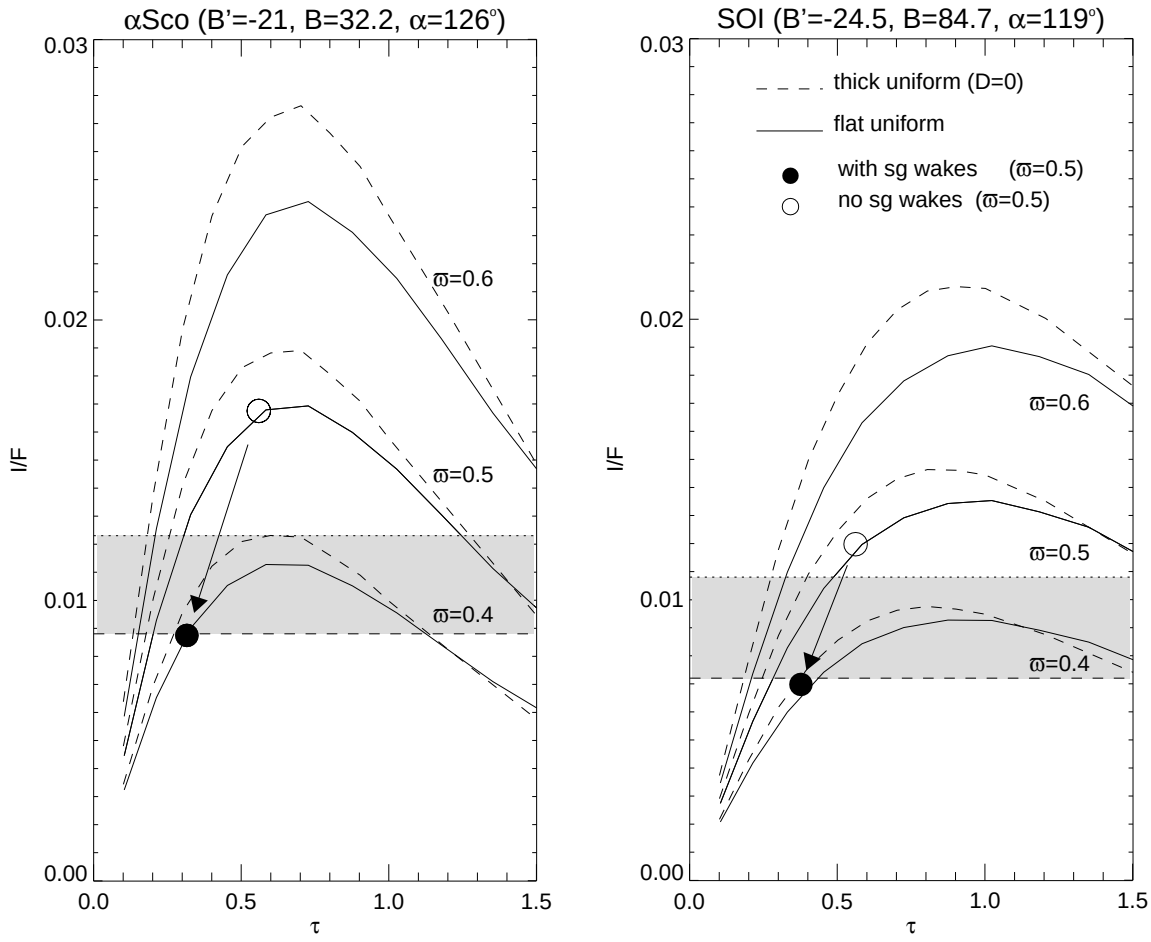

Figure S12: Photometric models of ring background brightness for the α Sco and SOI viewing geometries, assuming an $n = 3.09$ power law phase function with Bond albedo $\varpi = 0.4 - 0.6$. The curves refer to uniform ring models: solid curve to a vertically thin near-monolayer ring (a non-gravitating, non-perturbed dynamical simulation model with the velocity dependent coefficient of restitution from ref. (*18*)), and the dashed curve to a vertically thick ring (classical multilayer case with packing density $D \rightarrow 0$). The difference between these two curves illustrates the maximum effect local ring thickness/packing density may have on I/F. For comparison, arrows indicate the change in τ and I/F if self-gravity is included, while assuming an internal particle density of 450 kgm^{-3} which together with dynamical optical depth $\tau_{dyn} = 0.5$ and a particle radius of 1.67m yields a ring surface density of 500 kgm^{-2}. The same model including self-gravity was used in refs (*37*) and (*25*) to model the azimuthal asymmetry in Voyager and HST observations. The shaded regions indicate the typical background I/F in images (A_0 in Table S2) and the maximum I/F associated with the propeller ($A_0 + A_1$). Using the nominal phase function with $\varpi = 0.5$, the wake model I/F's are quite close to the observed background. As mentioned earlier, I/F levels for SOI images are probably more uncertain, and here we have used levels from Fig. S1 in ref. (*2*). In case of the Encke 'movie' sequence the model curves (not shown) are fairly similar to those for the α Sco geometry, except that I/F is slightly reduced due to the larger phase angle $\alpha = 162^\circ$: for $\varpi = 0.5$ the maximum I/F values would be 0.017 and 0.013 for the thick uniform and flat uniform models, respectively. In this case the observed background I/F =0.014 is close to uniform ring curves for, which is consistent with the indicated weakness of self-gravity wakes in this region.

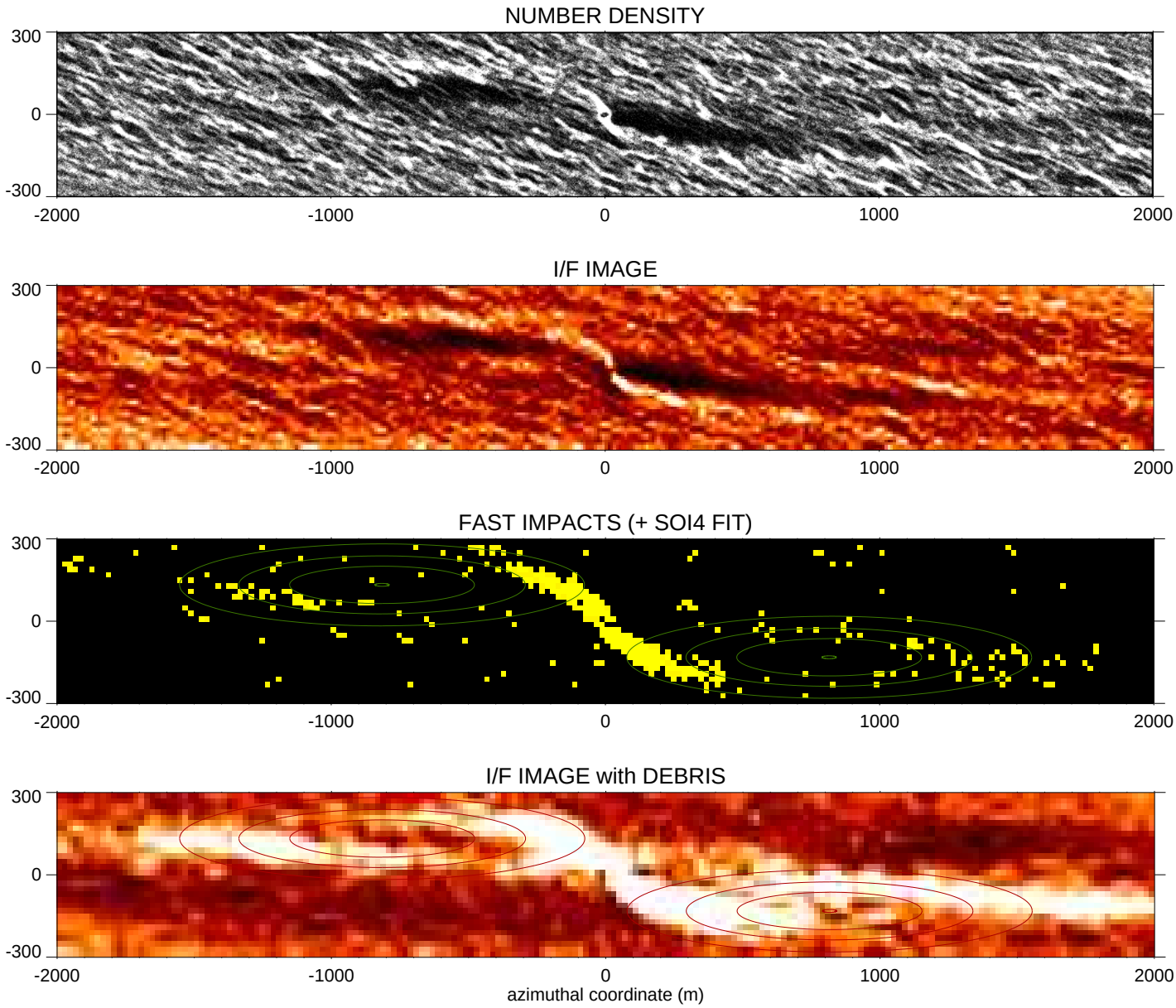

Figure S13: Simulation including self-gravity with an embedded 20 meter moonlet. A 6km $\times$ 1km co-moving ring patch at the distance $a = 130,000$km is used with N=345,000 identical particles. Parameter values for the particles are the same as in the wake model of Fig. S12; for the moonlet an internal density 600 kgm^{-3} is used. Only the centre-most 4000m by 600m region is shown. The uppermost panel shows the particle number density (superposition of 6 snapshots), while the next one shows a rectified I/F image constructed for the SOI geometry, using the same standard photometric parameters as in Fig. S12 (I/F range is 0 to 0.015). The third panel shows the location of fast impacts ($v_{\rm imp} > 1\,{\rm cm\,s}^{-1}$). Particle debris is assumed to be launched from these impact sites (the rms launch speed is one half of impact velocity, the launch directions are isotropic, and the probability of re-absorption is 25% in subsequent impacts). The last frame displays the combined I/F image including both particles and debris (the number density of debris is scaled to give an optical depth of 0.025, if averaged over the whole calculation region). The same power-law phase function is used for debris particles except with $\varpi = 0.9$. Contours illustrate the fit to the SOI4 propeller feature.

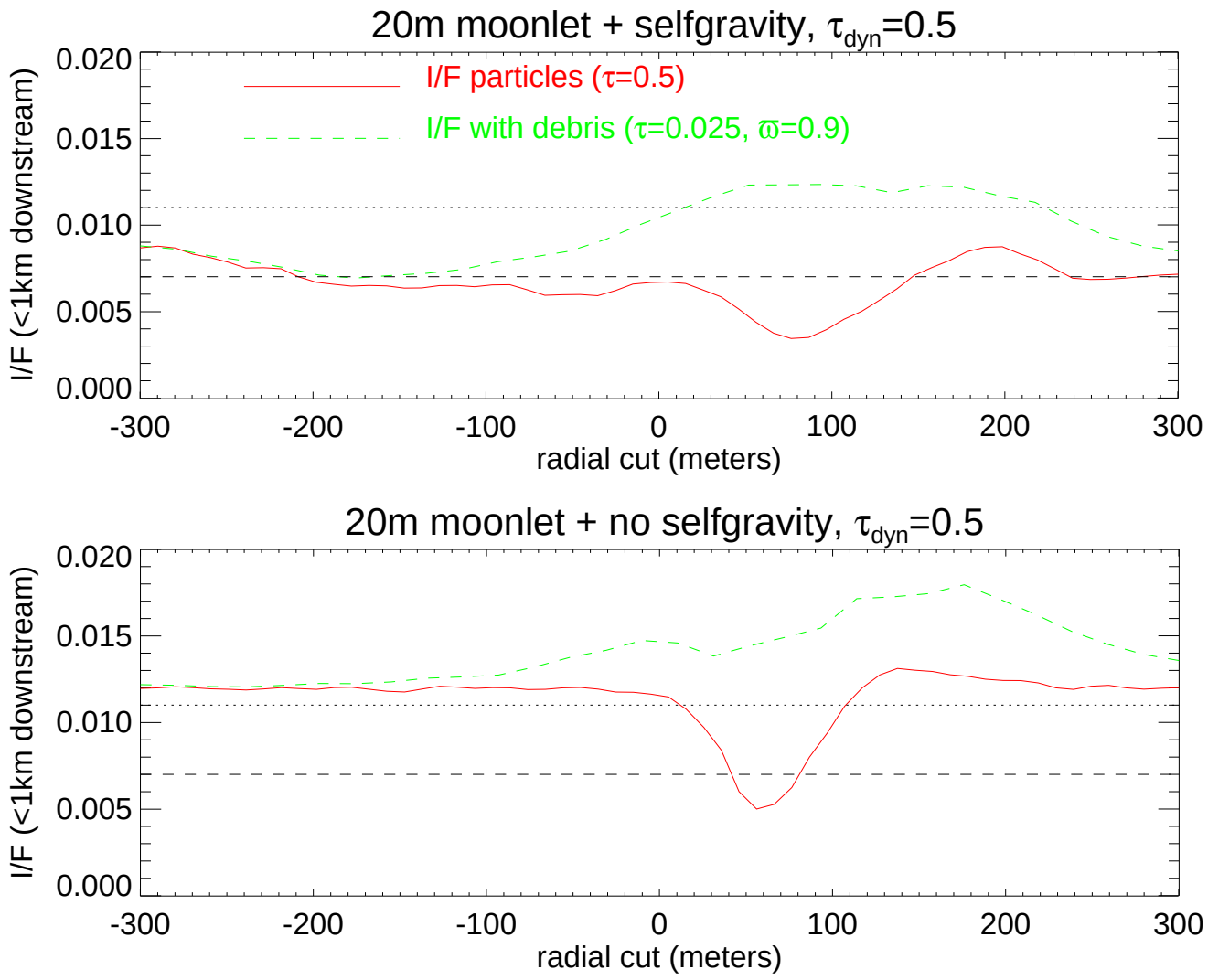

Figure S14: Radial cuts of the simulated propeller brightness profiles, averaged over the tangential zone 0.1 - 1km downstream of the moonlet. The upper frame corresponds to the self-gravitating 20 meter moonlet example of Fig. S16: the synthetic images with (green curve) and without impact-generated debris (red) are compared. The horizontal dashed lines indicate the observed background I/F and the maximum propeller brightness in the SOI images. Note how the debris helps to hide the dimmer gap, and, with the chosen mean optical depth $\tau_{\rm debris} = 0.0025$, rises the propeller I/F to the correct level (for the assumed debris albedo $\varpi = 0.9$; for $\varpi = 0.5$ about two-fold $\tau_{\rm debris}$ would be needed). The lower frame shows the same profiles for a non-gravitating simulation otherwise similar to Fig. S16. Although the background I/F is now higher due to the lack of self-gravity wakes (as for outer A ring images), the inclusion of debris (again scaled to $\tau_{\rm debris} = 0.0025$) enhances the propeller brightness in a similar fashion as in the presence of gravity wakes.

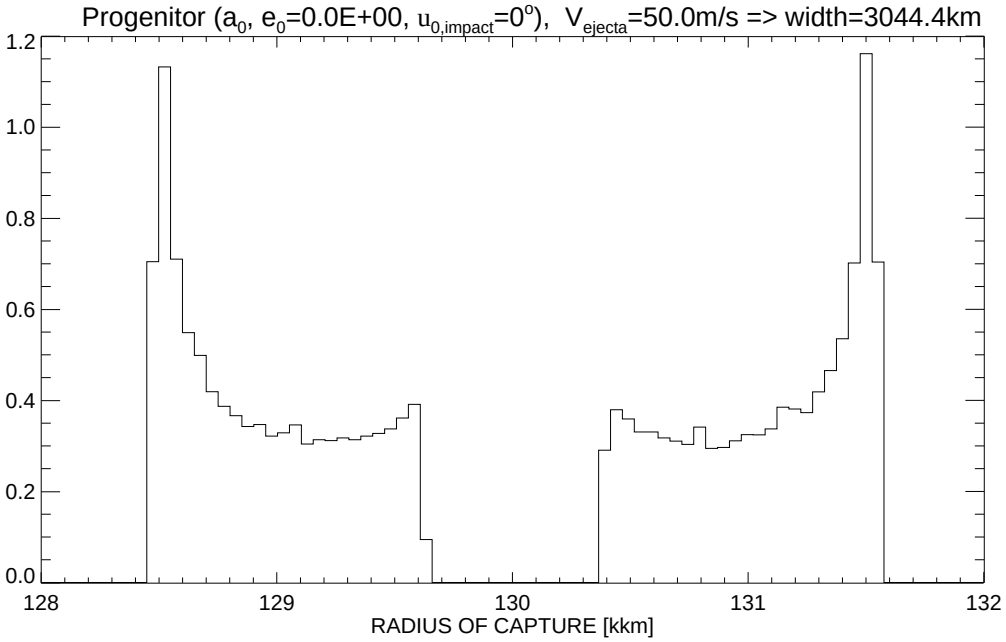

Figure S15: Distribution of the radii where the fragments are likely to be trapped by closing ring edges. A mean ejection speed $\langle v_{\rm ejecta} \rangle = 50\,{\rm m\,s^{-1}}$ is used and the target moon is on a circular orbit. Fragments are assumed to be trapped in the closing ring at their apocentre, if their semi-major axis is larger than the one of the progenitor moon, or at their pericentre, if their semi-major axis is smaller.

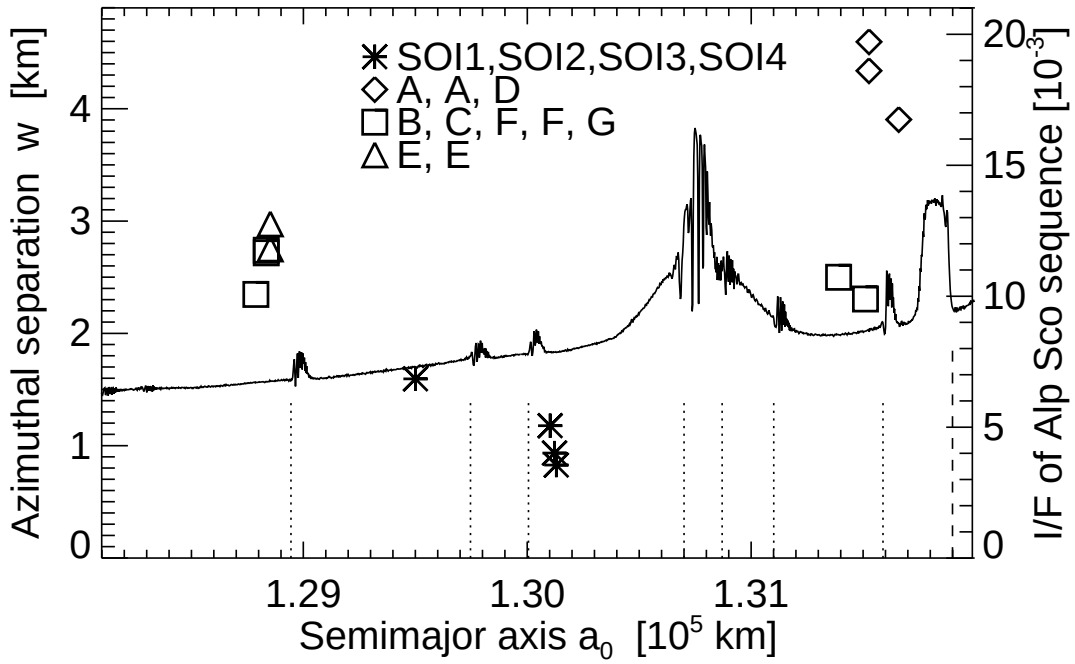

Figure S16: Location of propellers in the A ring. The vertical dotted lines at the bottom mark the density wave resonances: Prometheus 9:8, Pandora 8:7, Prometheus 10:9, Janus 5:4, Prometheus 11:10, Pandora 9:8, Prometheus 12:11, in that order from left to right, while the longer dashed line stands for Mimas 5:3 bending wave resonance.